

Article

Modeling and Testing Strategies for an Interconnected Four-Pole Magnetic Bearing

Domingos de Farias Brito David ¹, José Andrés Santisteban ² and Afonso Celso Del Nero Gomes ^{3,*}

¹ Mechanical Engineering Department, Universidade Federal Fluminense (UFF), Rua Passo da Pátria 156, Niterói 24210-240, Brazil; domingos@vm.uff.br (D.d.F.B.D.)

² Graduate Programs on Mechanical and on Electrical and Telecommunications Engineering, Universidade Federal Fluminense, Rua Passo da Pátria 156, Niterói 24210-240, Brazil; jasantisteban@vm.uff.br (J.A.S.)

³ Graduate Program on Electrical Engineering, COPPE-UFRJ, Universidade Federal do Rio de Janeiro, CP 68504, Rio de Janeiro 21945-970, Brazil

* Correspondence: nero@coep.ufrj.br; Tel.: +55-21-3986-8611

Received: 19 December 2016; Accepted: 12 June 2017; Published: 23 June 2017

Abstract: An unusual idea for the construction of active magnetic bearings has been recently discussed in the literature. Theoretical results predict a greater equivalent stiffness for it, when compared with traditional active magnetic bearings. The development of a mathematical model that allows these predictions and the use of recently-built prototypes for testing if the expectations hold true are the main goals of this paper.

Keywords: active magnetic bearings; reluctance forces; control of magnetic bearings; magnetic bearings stiffness; interconnected flux

1. Introduction

Conventional AMBs (active magnetic bearings) [1–3], here called Type A, are based on the structure shown in Figure 1. There are four “U-shaped electromagnets”, two for the x or horizontal direction and two in the y or vertical direction, resulting in four independent magnetic flux loops.

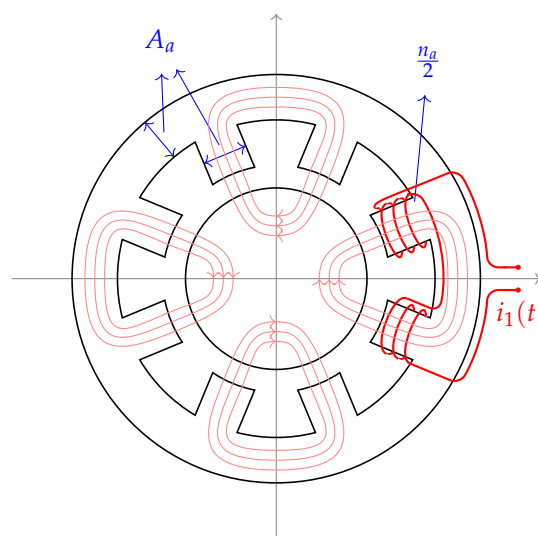


Figure 1. Type A, or traditional, configuration for active magnetic bearings (AMBs); windings are shown for the positive x direction only; there are no connections among the flux paths. Opposing pairs of windings along the x (y) direction control the horizontal (vertical) position.

The windings in the x and y direction are fed with currents $i_0 \pm i_x(t)$ and $i_0 \pm i_y(t)$; the constant current i_0 is the base, or bias, and the differential currents i_x and i_y will control the rotor position. Using basic reluctance concepts, the resultant forces f_x and f_y can be expressed in terms of these currents, the air magnetic permeability μ_0 , the total number of coils n_a , the cross-section area in the stator ferromagnetic material A_a and the nominal length h of the air gaps. After a standard linearization procedure [1] around the operating point $x = y = i_x = i_y = 0$, the forces generated by the Type A structure are shown in (1). Notice that the unconnected nature of the magnetic fluxes leads to uncoupled forces:

$$\left. \begin{aligned} f_x &= k_p^a x + k_i^a i_x \\ f_y &= k_p^a y + k_i^a i_y \end{aligned} \right\} \text{ where } \begin{cases} k_p^a = \mu_0 A_a n_a^2 i_0^2 / h^3 \\ k_i^a = \mu_0 A_a n_a^2 i_0 / h^2. \end{cases} \quad (1)$$

A different structure for magnetic bearings, here named Type B, is possible, with four windings that lead to interconnected magnetic loops, as depicted in Figure 2. This structure is found in the split-winding self-bearing motors researched in Brazil [4–10], among others. In that approach, to provide a simultaneous torque, alternate currents are injected into the windings; for AMBs, DC currents are considered.

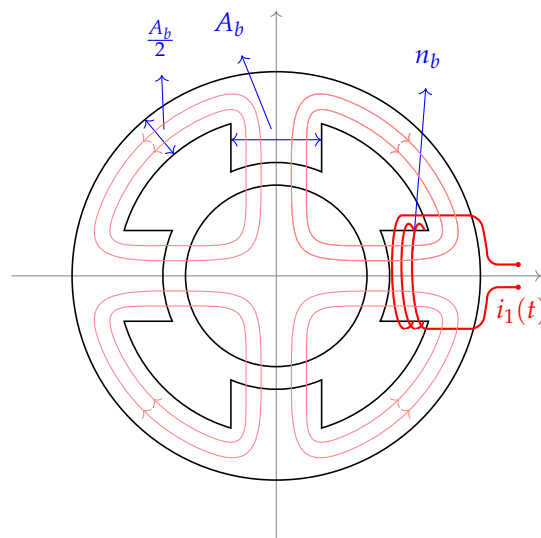


Figure 2. Type B, the proposed configuration for AMBs; windings are shown for the positive x direction only; the flux paths are interconnected. Opposing pairs of windings along the x (y) direction control the horizontal (vertical) position.

It is now appropriate to discuss, in a preliminary way, some aspects of this different geometry for AMBs. At first glance, it seems safe to state that Type B, with its four- “pole” stator structure, shows a cleaner and more compact design than Type A, which will probably result in more cost-effective manufacturing situations. It is also easy to accept that Type B offers more space for heat dissipation and that the flux losses in its coils are smaller.

It is clear that all of the very desirable Type B characteristics in the above paragraph do not represent true facts yet: they are only very reasonable conjectures that must be thoroughly tested before definite conclusions can be made. If all of these considerations turn out to be true, then the Type B geometry must be seen as a valid alternative to, if not as a better choice than, Type A for AMBs.

The main goal of this work is to discuss at some depth yet another aspect of this “reduced pole” geometry: its capability of generating restoring forces f_x and f_y that are potentially better for AMBs than those in the eight-“pole” case. It will be shown, in a theoretical way, that the linearized restoring forces for Type B are similar to those for Type A, shown in (1), but with a higher magnitude.

Is this ability of generating higher forces a desired characteristic for AMBs? This problem will also be addressed in this paper, with the help of examples. In order to assure that the theoretical conclusions for the four-pole geometry hold true in the real world, a series of laboratory tests is necessary. The final sections in this article deal with prototypes that have been built for Types A and B and consider the possible tests capable of comparing the force-generating performances of both structures.

This paper is based on ongoing research [11–13]. Its first stage, shown here, is based on theoretical considerations and on simulations; the last steps of this research, the important laboratory tests that can validate all of the initial considerations, are not ready yet, and will be presented in a future work. The material covered in this article is spread throughout the sections as follows. A mathematical model, based on elementary reluctance concepts, is detailed in Section 2, which tracks closely [11] and [12]. This model explains the generation of reluctance forces f_x and f_y in Type B bearings; the linearized final expressions for these forces show a decoupled nature, similar to those for Type A in (1). In addition, the position and current constants, k_p^b and k_i^b , are shown to have higher values than in the A case.

Section 3 presents analytical results and simulations on how increased values of $k_{p,i}^b$ affect the dynamics and control aspects of AMBs in a positive way [12]; simple examples that illustrate meaningful control situations are used. The prototypes built to the laboratory tests that will compare Types A and B are shown in Section 4; a mathematical model describing their dynamic behavior is developed. In Section 5, simulations of some control laws applied to the prototypes are made, and their results are discussed. The importance of this section is that the control laws used here will be the ones driving the prototypes in the real tests. Discussions about the future real tests, final comments and general considerations on what remains to be done are made in Section 6.

Other results are known in the literature with the Type B bearing concept. In [14], a Type B structure is used to minimize rotor vibrations; a non-linear expression for the bearing forces is mentioned by the authors. The Type B geometry is used in a magnetic force determination problem, in [15]; some steps are taken toward a reluctance model for the bearing forces. A patent for a Type B bearing was claimed and granted in [16], where some superior aspects of this structure are described. This short list is all that the authors could find.

None of the references above shows a detailed mathematical model, neither nonlinear nor linear, for the reluctance forces generated in a Type B structure, or any type of comparisons with Type A, like the ones presented in the next sections. The main contribution of this work is this mathematical model and the comparisons between the two possible types of AMBs.

2. Force Generation in Type B Bearings

A detailed study of the force generation in the flux interconnected structure (Type B) was presented in [6,11,12]; the main points are now repeated. The x and y components of a radial displacement of the rotor change the nominal gap width h , as shown in Figure 3.

To compensate the displacements, it is usual to apply differential currents [1] to the pairs of windings: the differential, or control, currents $i_x(t)$, for the x or horizontal direction, and $i_y(t)$, for the vertical direction, are added and subtracted to a base, or bias, current i_0 , a constant DC level. The total currents imposed at each winding are:

$$i_1(t) = i_0 + i_x(t) \quad \text{and} \quad i_3(t) = i_0 - i_x(t) \quad \text{for the } x \text{ direction,} \quad (2)$$

$$i_2(t) = i_0 + i_y(t) \quad \text{and} \quad i_4(t) = i_0 - i_y(t) \quad \text{for the } y \text{ direction.} \quad (3)$$

Light pink lines in Figure 2 represent the magnetic flux distribution caused by these currents. The reluctance forces depend on the magnetic fluxes ϕ_k , $k = 1, 2, 3, 4$, in the four air gaps with cross-section A_b :

$$f_x = \frac{\phi_1^2 - \phi_3^2}{2\mu_0 A_b} \quad \text{and} \quad f_y = \frac{\phi_2^2 - \phi_4^2}{2\mu_0 A_b}. \quad (4)$$

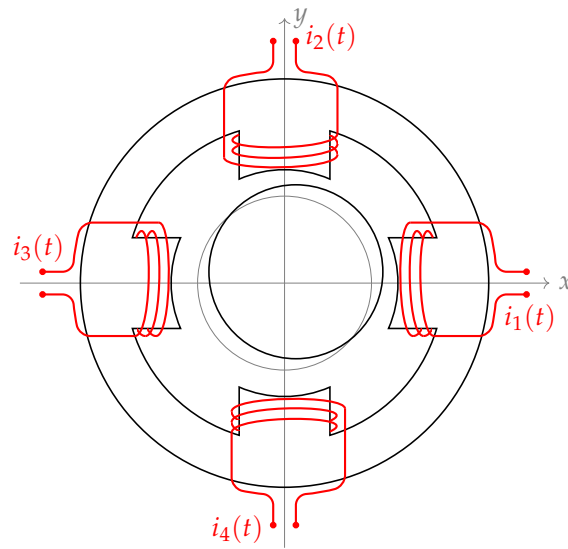


Figure 3. When the rotor moves x and y in the horizontal and vertical positions, the air gap widths change to $h - x$ in the right pole, $h + x$ (left pole), $h - y$ (upper pole) and $h + y$ (lower pole); the fluxes are not shown.

The ferromagnetic connections in Type B allow a current injected in any winding to cause fluxes in all four air gaps; Figure 4 illustrates the effects of i_1 in all four “poles”. If ϕ_{jk} denotes the flux in air gap j caused by a current in winding k , the total magnetic flux ϕ_1 in “Pole” 1 is a function of the fluxes $\phi_{11}, \phi_{12}, \phi_{13}, \phi_{14}$. Assuming no air or ferromagnetic losses and positive signs for fluxes headed to the rotating center, the total magnetic fluxes in the poles are:

$$\phi_1 = \phi_{11} + \phi_{12} - \phi_{13} + \phi_{14}, \quad \phi_2 = -\phi_{21} - \phi_{22} - \phi_{23} + \phi_{24}, \quad (5)$$

$$\phi_3 = -\phi_{31} + \phi_{32} + \phi_{33} + \phi_{34}, \quad \phi_4 = -\phi_{41} + \phi_{42} - \phi_{43} - \phi_{44}. \quad (6)$$

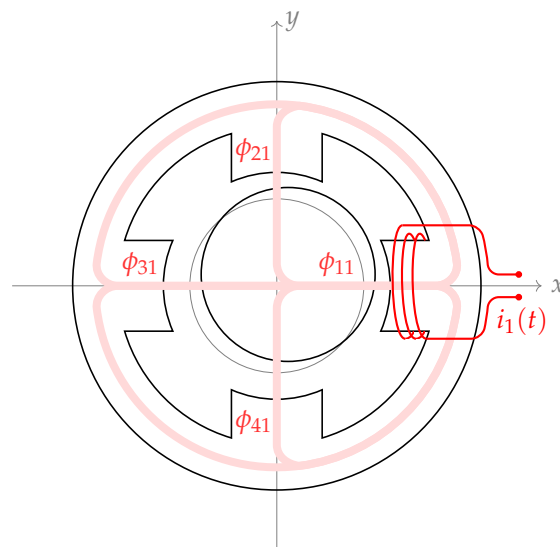


Figure 4. Magnetic flux distribution associated with i_1 in the Type B magnetic bearing; current injected only in Winding 1 causes fluxes in all air gaps.

For the determination of the ϕ_{jk} , let the magneto-motive force generated by i_1 be denoted by \mathcal{F}_1 and the reluctance of the air gaps in the four poles in Figure 3 by $\mathcal{R}_1, \mathcal{R}_2, \mathcal{R}_3$ and \mathcal{R}_4 . Recalling that

A_b is the cross-section area of the poles in Figure 2 and that the displacements h , x and y are explained in Figure 3, the reluctances are expressed by:

$$\mathcal{R}_1 = \frac{h-x}{\mu_0 A_b}, \quad \mathcal{R}_2 = \frac{h-y}{\mu_0 A_b}, \quad \mathcal{R}_3 = \frac{h+x}{\mu_0 A_b}, \quad \mathcal{R}_4 = \frac{h+y}{\mu_0 A_b}. \quad (7)$$

The equivalent circuit that models the magnetic flux situation in a Type B structure is shown in Figure 5.

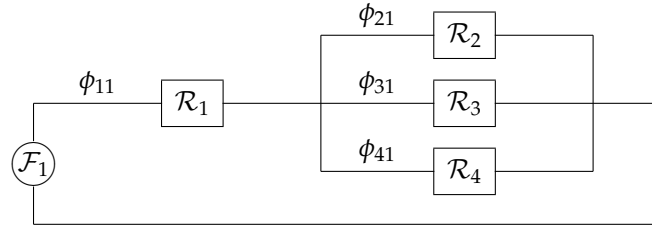


Figure 5. Magnetic flux equivalent circuit associated with current only in Winding 1 of the Type B magnetic bearing.

A simple way to extract information from magnetic circuits like the one in Figure 5 is by using the passive electric circuit analogy: fluxes are treated as currents; operations with reluctances are the same as those with resistances; and the usual operations allowed in Kirchoff’s rules are valid. It is easy to see that in the circuit under study, reluctance \mathcal{R}_1 is in series with the parallel combination of reluctance \mathcal{R}_2 , \mathcal{R}_3 and \mathcal{R}_4 . If \mathcal{R}_* denotes the equivalent reluctance of the parallel combination:

$$\frac{1}{\mathcal{R}_*} = \frac{1}{\mathcal{R}_2} + \frac{1}{\mathcal{R}_3} + \frac{1}{\mathcal{R}_4} = \frac{\mathcal{R}_3\mathcal{R}_4 + \mathcal{R}_2\mathcal{R}_4 + \mathcal{R}_2\mathcal{R}_3}{\mathcal{R}_2\mathcal{R}_3\mathcal{R}_4} \quad (8)$$

that easily leads to the value of \mathcal{R}_* . Therefore, the magnetic circuit in Figure 5 can be replaced by a single reluctance \mathcal{R}_1^e given by:

$$\mathcal{R}_1^e = \mathcal{R}_1 + \mathcal{R}_* = \mathcal{R}_1 + \frac{\mathcal{R}_2\mathcal{R}_3\mathcal{R}_4}{\mathcal{R}_3\mathcal{R}_4 + \mathcal{R}_2\mathcal{R}_4 + \mathcal{R}_2\mathcal{R}_3} \quad (9)$$

and, finally:

$$\mathcal{R}_1^e = \frac{\mathcal{R}_1\mathcal{R}_2\mathcal{R}_3 + \mathcal{R}_1\mathcal{R}_2\mathcal{R}_4 + \mathcal{R}_1\mathcal{R}_3\mathcal{R}_4 + \mathcal{R}_2\mathcal{R}_3\mathcal{R}_4}{\mathcal{R}_2\mathcal{R}_3 + \mathcal{R}_2\mathcal{R}_4 + \mathcal{R}_3\mathcal{R}_4}. \quad (10)$$

To avoid cumbersome formulas, some auxiliary variables are defined:

$$N = \mathcal{R}_1\mathcal{R}_2\mathcal{R}_3 + \mathcal{R}_1\mathcal{R}_2\mathcal{R}_4 + \mathcal{R}_1\mathcal{R}_3\mathcal{R}_4 + \mathcal{R}_2\mathcal{R}_3\mathcal{R}_4, \quad (11)$$

$$D_1 = \mathcal{R}_2\mathcal{R}_3 + \mathcal{R}_2\mathcal{R}_4 + \mathcal{R}_3\mathcal{R}_4, \quad D_2 = \mathcal{R}_1\mathcal{R}_3 + \mathcal{R}_1\mathcal{R}_4 + \mathcal{R}_3\mathcal{R}_4, \quad (12)$$

$$D_3 = \mathcal{R}_1\mathcal{R}_2 + \mathcal{R}_1\mathcal{R}_4 + \mathcal{R}_2\mathcal{R}_4, \quad D_4 = \mathcal{R}_1\mathcal{R}_2 + \mathcal{R}_1\mathcal{R}_3 + \mathcal{R}_2\mathcal{R}_3. \quad (13)$$

Since $\mathcal{F}_1 = n_b i_1$, algebraic operations lead to expressions for the fluxes associated with $i_1 = i_0 + i_x$ imposed on the winding in Pole 1 of Figure 3:

$$\phi_{11} = \frac{\mathcal{F}_1}{\mathcal{R}_1^e} = n_b(i_0 + i_x) \frac{D_1}{N}, \quad \phi_{21} = n_b(i_0 + i_x) \frac{\mathcal{R}_3\mathcal{R}_4}{N}, \quad (14)$$

$$\phi_{31} = n_b(i_0 + i_x) \frac{\mathcal{R}_2\mathcal{R}_4}{N}, \quad \phi_{41} = n_b(i_0 + i_x) \frac{\mathcal{R}_2\mathcal{R}_3}{N}. \quad (15)$$

The same procedure, repeated for currents i_2, i_3, i_4 imposed at the windings in Poles 2, 3 and 4 in Figure 3 results in:

$$\begin{aligned} \phi_{12} &= n_b(i_0 + i_y) \frac{\mathcal{R}_3 \mathcal{R}_4}{N}, & \phi_{22} &= n_b(i_0 + i_y) \frac{D_2}{N}, & \phi_{32} &= n_b(i_0 + i_y) \frac{\mathcal{R}_1 \mathcal{R}_4}{N}, & \phi_{42} &= n_b(i_0 + i_y) \frac{\mathcal{R}_1 \mathcal{R}_3}{N}, \\ \phi_{13} &= n_b(i_0 - i_x) \frac{\mathcal{R}_2 \mathcal{R}_4}{N}, & \phi_{23} &= n_b(i_0 - i_x) \frac{\mathcal{R}_1 \mathcal{R}_4}{N}, & \phi_{33} &= n_b(i_0 - i_x) \frac{D_3}{N}, & \phi_{43} &= n_b(i_0 - i_x) \frac{\mathcal{R}_1 \mathcal{R}_2}{N}, \\ \phi_{14} &= n_b(i_0 - i_y) \frac{\mathcal{R}_2 \mathcal{R}_3}{N}, & \phi_{24} &= n_b(i_0 - i_y) \frac{\mathcal{R}_1 \mathcal{R}_3}{N}, & \phi_{34} &= n_b(i_0 - i_y) \frac{\mathcal{R}_1 \mathcal{R}_2}{N}, & \phi_{44} &= n_b(i_0 - i_y) \frac{D_4}{N}. \end{aligned}$$

The total fluxes ϕ_k for $k = 1, 2, 3, 4$ can be determined by substituting the previous values of the partial fluxes ϕ_{jk} in Equations (5) and (6). Then, with the help of (4), the total reluctance forces generated in a Type B magnetic bearing can be expressed as:

$$f_x = \frac{\mu_0 A_b n_b^2}{2} q_x(h, x, y, i_0, i_x, i_y) \quad \text{and} \quad f_y = \frac{\mu_0 A_b n_b^2}{2} q_y(h, x, y, i_0, i_x, i_y) \quad (16)$$

where $q_{x,y}$ are complicated functions of their arguments:

$$q_x(h, x, y, i_0, i_x, i_y) = \frac{N_1^2 - N_2^2}{\Delta^2} \quad \text{and} \quad q_y(h, x, y, i_0, i_x, i_y) = \frac{N_3^2 - N_4^2}{\Delta^2} \quad (17)$$

with

$$\begin{aligned} N_1 &= (i_1 + i_2)\Delta_1 + (i_1 - i_3)\Delta_2 + (i_1 + i_4)\Delta_3, & N_2 &= (i_3 - i_1)\Delta_2 + (i_2 + i_3)\Delta_4 + (i_3 + i_4)\Delta_5, \\ N_3 &= (i_1 + i_2)\Delta_1 + (i_2 + i_3)\Delta_4 + (i_2 - i_4)\Delta_6, & N_4 &= (i_1 + i_4)\Delta_3 + (i_3 + i_4)\Delta_5 - (i_2 - i_4)\Delta_6. \end{aligned}$$

The currents i_k are defined in Equations (2) and (3); if the distances $h \pm x$ and $h \pm y$ are denoted by δ_x^\pm and δ_y^\pm , the Δ s above are:

$$\begin{aligned} \Delta_1 &= \delta_x^+ \delta_y^+, & \Delta_2 &= \delta_y^+ \delta_y^-, & \Delta_3 &= \delta_x^+ \delta_y^- \\ \Delta_4 &= \delta_x^- \delta_y^+, & \Delta_5 &= \delta_x^- \delta_y^-, & \Delta_6 &= \delta_x^+ \delta_x^- \\ \Delta &= \delta_x^- \delta_y^- \delta_x^+ + \delta_x^- \delta_y^- \delta_y^+ + \delta_x^- \delta_x^+ \delta_y^+ + \delta_y^- \delta_x^+ \delta_y^+. \end{aligned}$$

The complexity of the above formulas makes the linearization of (16) a hard task. Considering that the AMB operates around a point $P_0 = (x, y, i_x, i_y)_0 = (0, 0, 0, 0)$, the use of symbolical computation, or even a pen on paper procedure, allows the calculation of the partial derivatives:

$$\left. \frac{\partial q_x}{\partial x} \right|_{P_0} = \frac{4i_0^2}{h^3} \quad \left. \frac{\partial q_x}{\partial y} \right|_{P_0} = 0 \quad (18)$$

$$\left. \frac{\partial q_x}{\partial i_x} \right|_{P_0} = \frac{4i_0}{h^2} \quad \left. \frac{\partial q_x}{\partial i_y} \right|_{P_0} = 0. \quad (19)$$

If a similar procedure is made for q_y , the combined results lead to the linear expressions for the Type B structure forces:

$$\left. \begin{aligned} f_x &= k_p^b x + k_i^b i_x \\ f_y &= k_p^b y + k_i^b i_y \end{aligned} \right\} \text{where} \left\{ \begin{aligned} k_p^b &= 2\mu_0 A_b n_b^2 i_0^2 / h^3 \\ k_i^b &= 2\mu_0 A_b n_b^2 i_0 / h^2. \end{aligned} \right. \quad (20)$$

Two remarkable aspects are to be noted when these expressions are compared with the ones in (1): (a) even though the fluxes are interconnected in a Type B structure, the forces are decoupled, exactly

as they were in Type A; (b) a factor of two appears in the formulas above for the $k_{p,i}^b$, which was not present in Case A.

In the above developments, an underlying assumption is made: there is no magnetic saturation. What happens when both types are saturated? This is a pertinent question that cannot be answered with theoretical tools: extensive laboratory tests would have to be done.

3. Theoretical Comparisons

Assuming the same outside diameter of the stator, the following characteristics can be identified for the Type B active magnetic bearing when it is compared with Type A:

1. The position and current constants k_p^b and k_i^b in (20) are two-times bigger than their counterparts k_p^a and k_i^a in Equation (1);
2. the cross-section area A_b can be chosen greater than A_a ; it is reasonable to have $A_b \approx 2A_a$;
3. the number of coils n_b can, possibly, be larger than n_a .

The net conclusion is: the position (k_p) and current (k_i) constants for Type B AMBs have values at least two-times higher than in Case A. Depending on the design aspects (A_b and n_b), even higher rates can be achieved. How much can these constants be increased? The magnetic saturation seems to be the limit. Higher valued coefficients mean, at first sight, higher forces for the same input currents and displacements and a different dynamic behavior for Type B. Are these effects beneficial in the AMB performance? Are they sound advantages?

To evaluate the effects of k_b and k_i in an AMB operation, a theoretical analysis was applied, in [12], to a simple, but meaningful, control problem, where many aspects of the real-life functioning of AMBs are present. That material is summarized in Figure 6: a particle moving without friction in a horizontal, rectilinear path is to be positioned.

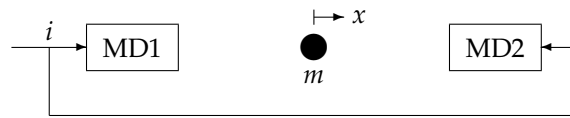


Figure 6. The particle position $x(t)$ is to be controlled by injecting currents in the magnetic devices MD1 and MD2; only horizontal and frictionless movements are considered.

The magnetic devices MD1 and MD2 apply a resultant force $f(t) = k_p x(t) + k_i i(t)$ on the sphere, where i is a control current and x is the displacement. A controller is desired, for driving $x(t)$ to zero for all possible initial conditions, and in the eventual presence of constant, horizontal disturbance forces d . A mathematical model can be found with a simple application of Newton's law: $f(t) + d(t) = m\ddot{x}(t)$. The linear nature of f leads to $m\ddot{x}(t) - k_p x(t) = k_i i(t) + d(t)$, which can be expressed, with the use of Laplace transforms, as $(ms^2 - k_p)X(s) = k_i I(s) + D(s)$. The particle position (its Laplace transform) is, therefore, given by:

$$X(s) = \frac{k_i I(s) + D(s)}{ms^2 - k_p} = \frac{(1/m)}{s^2 - (k_p/m)} (k_i I(s) + D(s)) = G(s)(k_i I(s) + D(s)) \quad (21)$$

where $G(s)$ is called the plant transfer function. The controller's output is the current i and its input is the error signal $e = r - x$ where r is an external reference that indicates the desired behavior of x (in this case, $r = 0$). If $C(s)$ is the controller transfer function, then, using the Laplace transforms:

$$I(s) = C(s)E(s) = C(s)(R(s) - X(s)). \quad (22)$$

Combining (21) and (22), it is possible, after some direct algebraic manipulations, to see how the overall output x depends on the command input r and the disturbance input d :

$$X(s) = T_c(s)R(s) + T_d(s)D(s) \text{ where } T_c(s) = \frac{k_i C(s)G(s)}{1 + k_i C(s)G(s)} \text{ and } T_d(s) = \frac{G(s)}{1 + k_i C(s)G(s)}. \quad (23)$$

The command transfer function $T_c(s)$ measures the effect of the reference input r on the closed loop behavior; it is common to say that controllers are designed to make $T_c(s)$ as close to unity as possible, meaning that x must be as close to r as possible. The disturbance transfer function $T_d(s)$ indicates how the controlled output x depends on d ; controllers should, ideally, make $T_d(s)$ as close to zero as possible. Block diagrams, widely used in control studies, are a very convenient tool for presenting expressions like (21) and (22) in an easy to understand graphical way. The block diagram in Figure 7 models the use of a controller $C(s)$ in the particle problem.

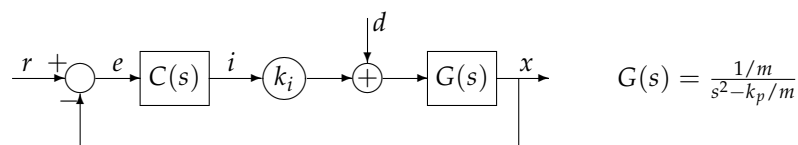


Figure 7. Block diagram showing the plant dynamics, in the transfer function $G(s)$, and a closed loop control scheme with a controller $C(s)$.

It is possible, using the simple rules of the so-called block diagrams algebra, to extract $T_c(s)$ and $T_d(s)$ from block diagrams, which is easier and faster than the above manipulations leading to (23). These last paragraphs cover basic control aspects and can be found in almost all textbooks on the field.

A stabilizing PD controller $C(s) = \alpha s + \beta$ guarantees that initial displacements $x(0) \neq 0$ are corrected, when $d = 0$. The speed of convergence depends on the closed loop poles, which are functions of α and β . The effects of extra horizontal forces d on $x(t)$ can be evaluated by $X_d(s) = T_d(s)D(s)$, where $T_d(s)$ is the disturbance transfer function. For this problem, the effect of d on x is described, with the results in (23) and using $C(s) = \alpha s + \beta$ for the PD controller, by:

$$T_d(s) = \frac{G(s)}{1 + k_i C(s)G(s)} = \frac{1/m}{s^2 + a_1 s + a_0}$$

where the characteristic polynomial coefficients are: $a_1 = \alpha k_i / m$ and: $a_0 = (\beta k_i - k_p) / m$. The steady state influence of disturbances, when $r = 0$, is measured by $\rho = \lim_{t \rightarrow \infty} x(t)$. Assuming closed loop stability, an important property of the Laplace transforms (the final value theorem) says that: $\rho = \lim_{s \rightarrow 0} sX(s) = \lim_{s \rightarrow 0} sT_d(s)D(s)$. For constant disturbances $D(s) = d_0/s$ this leads to

$$\rho = \lim_{s \rightarrow 0} sT_d(s) \frac{d_0}{s} = d_0 T_d(0) = \frac{d_0}{\beta k_i - k_p}. \quad (24)$$

The well-known fact that PD controllers do not completely reject ($\rho = 0$) constant disturbances becomes apparent. However, Equation (24) tells more: for a fixed, stabilizing controller, ρ decreases when k_p and k_i increase by the same factor. In other words, if the position and current coefficients in a magnetic force generation law are both increased by the same amount, the resulting PD control is less sensitive to constant disturbances, and this characterizes a better, stiffer suspension.

Since a full steady state rejection of constant disturbances can be achieved by PID controllers, consider now $C(s) = \alpha s + \beta + \gamma/s$. The new disturbance transfer function $T_d(s)$ is:

$$T_d(s) = \frac{s/m}{s^3 + a_2s^2 + a_1s + a_0} \quad \text{with} \quad \begin{cases} a_2 = \alpha k_i/m \\ a_1 = (\beta k_i - k_p)/m \\ a_0 = \gamma k_i/m. \end{cases}$$

Because each coefficient depends on a single controller parameter, the closed loop poles can be arbitrarily assigned. A simple calculation shows that complete rejection ($\rho = 0$) of step disturbances is indeed achieved by the PID controller.

In order to feel the performance details of the situation, a simulation was performed. The numerical values, in the SI system, $m = 4$, $k_i^0 = 200$ and $k_p^0 = 200,000$ were used. A PID controller that assigns all of the closed loop poles at -10 was calculated: $\alpha = 3/5$, $\beta = 10,006$ and $\gamma = 20$. An initial displacement of 1 cm was imposed on the sphere, and in less than 1 s, it returned to the desired rest position $x = 0$. After stabilization, a constant disturbance ($d_0 = 40$ N) was applied and successfully rejected. Figure 8 shows the curves for different values of the k_i and k_p constants: (k_i^0, k_p^0) , $(2k_i^0, 2k_p^0)$, $(4k_i^0, 4k_p^0)$ and $(8k_i^0, 8k_p^0)$.

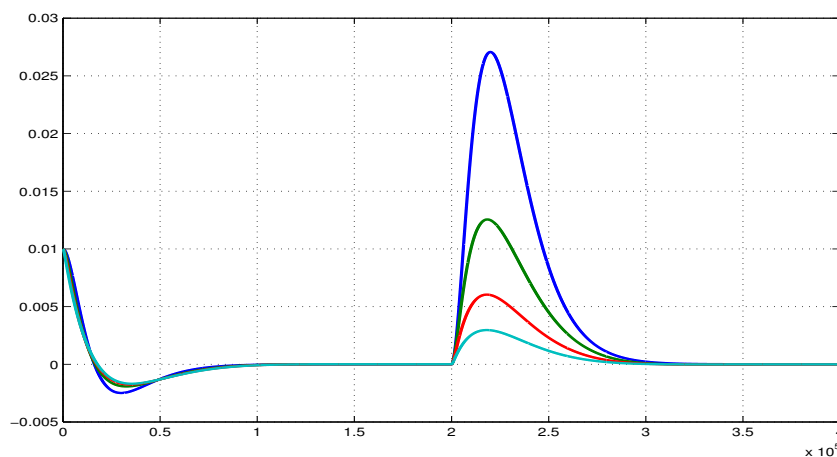


Figure 8. Sphere positioning with PID control for several values of the magnetic constants k_p and k_i . The vertical axis displays the sphere displacement x , in meters; time t is in the horizontal axis, with a total simulation time of 4 s, using 10^5 points per second. The highest rising, dark blue curve refers to the nominal values (NV) k_p^0 and k_i^0 ; twice the NV leads to the dark green (second highest rising) curve; four- and eight-times the NV generate the next curves, red and light blue.

All curves are very similar in the first 2 s, implying that high or low values for the magnetic constants are not crucial in the stabilizing stage. However, when constant disturbance rejection is needed, better transient behaviors are a direct consequence of higher values in k_p and k_i .

The conclusions of this simple example in [12] are valid in much more general situations, involving real-world applications of practical interest. Additionally, these conclusions are: increasing the values of the magnetic force constants k_p and k_i is a highly desirable goal in the AMB field.

4. Prototype Building and Models

The final conclusions of Sections 2 and 3 are that the interconnected fluxes in the Type B structure increase the values of the magnetic force constants k_p and k_i . How sure can one be about the theoretical tools used in those developments? The best possible way to answer this question is by constructing

and testing prototypes in an exhaustive way. Only after this stage will the ideas proposed here be validated; or not. Two prototypes, one for Type A and the other for Type B, have been constructed; Figure 9 shows a top view of them. A vertical rotor with a large, perforated upper disk will fill the above pieces; the same Figure 9, in the center, shows a view of a mounted kit, with the rotor inserted in the carcass with the stators. The upper disk's sole purpose is to determine whether Type B is really a stiffer AMB than Type A; see Section 5. This is because it can generate, in an easy way, as explained in Section 4.4, harmonic disturbances.



Figure 9. Top view of Prototypes A, on the left, and B, on the right; notice the eight “poles” in Type A and only four “poles” in Type B. A mounted kit is shown in the center, with a vertical rotor inserted in one of the carcasses. The perforated disk built in the upper position is used for mass unbalance tests.

The details of the vertical part are depicted in Figure 10. The bottom part is a mechanical bearing to prevent vertical movements; just above it there is the rotor of a two-phase induction motor for spinning the shaft. Next comes the AMB rotor, the same for Types A and B, and the sensors’ target. A disk with holes perforated near its edge lies on the upper part.

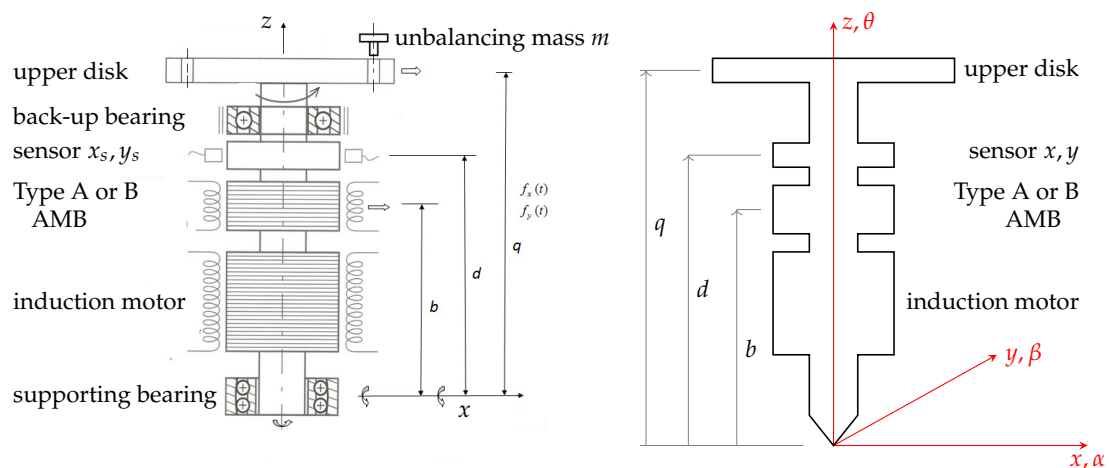


Figure 10. Vertical rotor’s aspects and dimensions, in the left part. In the right half, a simplified representation of its basic geometric aspects and dimensions.

Traditional procedures, like those in [1,3] and Chapter 4 in [2], will be used to find mathematical models for the prototypes. The self-aligning, supporting bearing at the bottom, while allowing angular movements in any direction, provides a fixed point for the rotor. An inertial reference system is placed at this location; axes x and y lie in the horizontal plane, and z marks the vertical direction. The positive

angles α , β and θ can be found by using the right-hand rule on x , y and z . The right half of Figure 10 sketches the situation; the supporting and back-up bearings are not shown.

Assuming a rigid and homogeneous rotor, the center of mass displacements can be determined by the angles α and β , and a full dynamic model can be obtained from the rotational equations alone. Denoting the angular moments of inertia around the three axes by I_x , I_y and I_z , symmetry considerations assure that $I_x = I_y = J$. In the classical Newton–Lagrange framework, the dynamic equations for rotations are:

$$J\ddot{\beta}(t) - \omega I_z \dot{\alpha}(t) = E_\beta \quad (25)$$

$$J\ddot{\alpha}(t) + \omega I_z \dot{\beta}(t) = E_\alpha \quad (26)$$

where $\omega = \dot{\theta}$ is the rotor angular velocity and $E_{\beta,\alpha}$ express all external actions generating torques. The main equations above can be displayed in a vector form:

$$J \begin{bmatrix} \ddot{\beta} \\ -\ddot{\alpha} \end{bmatrix} + \begin{bmatrix} 0 & \omega I_z \\ -\omega I_z & 0 \end{bmatrix} \begin{bmatrix} \dot{\beta} \\ -\dot{\alpha} \end{bmatrix} = \begin{bmatrix} E_\beta \\ -E_\alpha \end{bmatrix}. \quad (27)$$

Defining the angular position vector \mathbf{p} and the external excitation vector \mathbf{E} as:

$$\mathbf{p} = \begin{bmatrix} \beta \\ -\alpha \end{bmatrix} \quad \text{and} \quad \mathbf{E} = \begin{bmatrix} E_\beta \\ -E_\alpha \end{bmatrix} \quad (28)$$

the rotor dynamics is described by:

$$J\ddot{\mathbf{p}}(t) + G\dot{\mathbf{p}}(t) = \mathbf{E}(t) \quad (29)$$

where J is the inertia coefficient (or the inertia matrix $J\mathbf{I}_2$) and G is the gyroscopic matrix:

$$G = \begin{bmatrix} 0 & \omega I_z \\ -\omega I_z & 0 \end{bmatrix} = \omega I_z \begin{bmatrix} 0 & 1 \\ -1 & 0 \end{bmatrix}. \quad (30)$$

External torques may come from many different sources, four of which are considered in this paper: the magnetic (\mathbf{E}_m), gravitational (\mathbf{E}_g), supporting bearing (\mathbf{E}_a) and disturbance or mass unbalance (\mathbf{E}_d) torques.

$$\mathbf{E} = \mathbf{E}_m + \mathbf{E}_g + \mathbf{E}_a + \mathbf{E}_d \quad (31)$$

4.1. Magnetic Excitation

Considering x_b and y_b the rotor displacements at the AMB position, the forces generated in each direction are:

$$f_x = k_p x_b + k_i i_x \quad \text{and} \quad f_y = k_p y_b + k_i i_y \quad (32)$$

where the differential currents i_x and i_y were discussed in Section 1, and the coefficients $k_{p,i}$ can refer to either Type A or B. Assuming rigidity and small angular displacements:

$$\beta \approx \sin \beta = \frac{x_b}{b} \quad \text{and} \quad \alpha \approx \sin \alpha = \frac{-y_b}{b}$$

which lead to $x_b \approx b\beta$ and $y_b \approx b(-\alpha)$. Equation (32) becomes:

$$f_x = bk_p \beta + k_i i_x \quad \text{and} \quad f_y = bk_p(-\alpha) + k_i i_y.$$

These forces cause torques $P_\beta = bf_x \cos \beta$ and $P_\alpha = -bf_y \cos \alpha$. Assuming, again, rigidity and small angular displacements: $\cos \beta \approx 1$ and $\cos \alpha \approx 1$, which lead to $P_\beta = bf_x$ and $P_\alpha = -bf_y$. These magnetic torques can be expanded as:

$$P_\beta = b^2k_p\beta + bk_i i_x \quad \text{and} \quad -P_\alpha = b^2k_p(-\alpha) + bk_i i_y.$$

If $E_m = [P_\beta \ -P_\alpha]^T$ is the magnetic external excitation vector and $\mathbf{u} = [i_x \ i_y]^T$ is the external input or control vector, a concise expression can be written:

$$\mathbf{E}_m = b^2k_p\mathbf{p} + bk_i\mathbf{u}. \tag{33}$$

4.2. Gravitational Excitation

Since α and β are small angles, the torques caused by the rotor weight acting at its center of mass are negligible:

$$\mathbf{E}_g \approx 0. \tag{34}$$

This is usually the case with vertical rotors; for horizontal ones, gravity must be considered.

4.3. Supporting Bearing Excitation

The supporting bearing has a viscous damper effect; if C_a is the viscous constant, the torques are modeled by $P_\beta = -C_a\dot{\beta}$ and $P_\alpha = -C_a\dot{\alpha}$, and the external excitation contribution is:

$$\mathbf{E}_a = \begin{bmatrix} P_\beta \\ -P_\alpha \end{bmatrix} = -C_a \begin{bmatrix} \dot{\beta} \\ -\dot{\alpha} \end{bmatrix} \implies \mathbf{E}_a = -C_a\dot{\mathbf{p}} \tag{35}$$

4.4. Mass Unbalance Excitation

Rotors with a homogeneous mass distribution are assumed in the mathematical model. When, and if, this is not true, unexpected torques appear, acting as disturbances. If these actions are not considered when designing control laws, their effects, sometimes, can be unpleasant and even unacceptable. The upper disk in the considered rotor has 12 holes near the outer edge, placed in a symmetrical way, to preserve the body homogeneity. A small mass m in one of the holes, as shown in Figure 11, will act on the rotor with a centrifugal force $mr\dot{\theta}^2 = mr\omega^2$, causing an intentional disturbance.

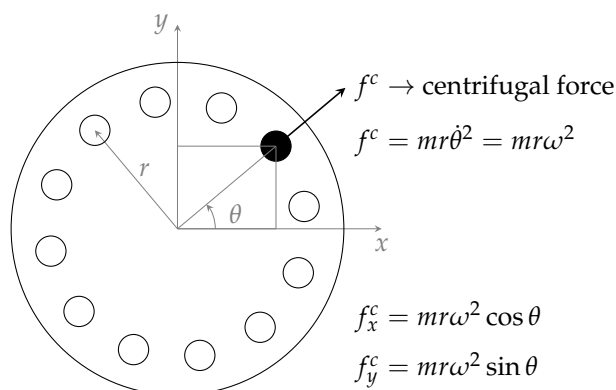


Figure 11. Top view of the upper disk with an extra mass m filling one of the holes; the centrifugal force is projected on the x and y axes.

The projections of the centrifugal force on the x and y directions are: $f_x^c = mr\omega^2 \cos \theta$ and $f_y^c = mr\omega^2 \sin \theta$. Since $\theta(t) = \omega t$, the disturbance torques generated by the unbalanced mass are: $P_\beta = mrq\omega^2 \cos \omega t$ and $P_\alpha = mrq\omega^2 \sin \omega t$. The mass unbalance external excitation contribution is

$$E_d = \begin{bmatrix} P_\beta \\ -P_\alpha \end{bmatrix} = mrq\omega^2 \begin{bmatrix} \cos \omega t \\ -\sin \omega t \end{bmatrix} = \Delta v(t) \tag{36}$$

where:

$$\Delta = mrq\omega^2 \quad \text{and} \quad v(t) = \begin{bmatrix} \cos \omega t \\ -\sin \omega t \end{bmatrix} \tag{37}$$

are, respectively, the disturbance coefficient and the disturbance input vector.

4.5. Detailed Dynamic Equations

Entering Expressions (33)–(36) in Equation (29) leads, after rearranging terms, to:

$$J\ddot{\mathbf{p}}(t) + (G + C_a I_2) \dot{\mathbf{p}}(t) - b^2 k_p \mathbf{p}(t) = b k_i \mathbf{u}(t) + \Delta v(t). \tag{38}$$

It is convenient to rewrite this equation in terms of x_s and y_s , the positions measured by the sensors. Rotor rigidity, small angles and geometry considerations guarantee that:

$$\beta \approx \sin \beta = \frac{x_s}{d} \quad \text{and} \quad \alpha \approx \sin \alpha = \frac{-y_s}{d}$$

which leads to $x_s = d\beta$ and $y_s = d(-\alpha)$. If the sensor measurements vector is denoted by $\mathbf{p}_s = [x_s \ y_s]^T$, then:

$$\begin{bmatrix} x_s \\ y_s \end{bmatrix} = d \begin{bmatrix} \beta \\ -\alpha \end{bmatrix} \implies \mathbf{p}_s = d\mathbf{p} \tag{39}$$

Multiplying (38) by d from the left, using (39) and dividing by J , we reach an expression in terms of the sensor positions:

$$\ddot{\mathbf{p}}_s + G_e \dot{\mathbf{p}}_s - K_e \mathbf{p}_s = B_2 \mathbf{u} + D_2 v \tag{40}$$

where the parameters are:

$$G_e = J^{-1} (G + C_a I_2) = J^{-1} \begin{bmatrix} C_a & \omega I_z \\ -\omega I_z & C_a \end{bmatrix}, \quad K_e = J^{-1} b^2 k_p, \quad B_2 = J^{-1} b d k_i, \quad D_2 = J^{-1} m r q d \omega^2. \tag{41}$$

In order to express the system dynamic behavior in the state space, the state variables:

$$\mathbf{x} = \begin{bmatrix} \mathbf{p}_s \\ \dot{\mathbf{p}}_s \end{bmatrix} = \begin{bmatrix} x_s \\ y_s \\ \dot{x}_s \\ \dot{y}_s \end{bmatrix}$$

can be chosen; Equation (40) becomes:

$$\dot{\mathbf{x}}(t) = A\mathbf{x}(t) + B\mathbf{u}(t) + Dv(t) \tag{42}$$

where x, u and v have been previously defined, A is a 4×4 matrix and B, D are 4×2 matrices structured as:

$$A = \begin{bmatrix} 0 & I \\ A_{21} & A_{22} \end{bmatrix}, \quad B = \begin{bmatrix} 0 \\ B_2 \end{bmatrix}, \quad D = \begin{bmatrix} 0 \\ D_2 \end{bmatrix} \quad (43)$$

where the 2×2 blocks are:

$$A_{21} = K_e I = J^{-1} b^2 k_p I_2 = A_{21}(k_p), \quad A_{22} = -G_e = -J^{-1} \begin{bmatrix} C_a & \omega I_z \\ -\omega I_z & C_a \end{bmatrix} = A_{22}(\omega), \quad (44)$$

$$B_2 = J^{-1} b d k_i I_2 = B_2(k_i), \quad D_2 = J^{-1} m r q d \omega^2 I_2 = D_2(m, \omega). \quad (45)$$

It is important to notice that Equation (42) models a linear system that is time invariant only for a fixed rotational speed, because A_{22} depends on ω .

5. Prototype Simulations

The simulations in this section do not cover the normal operation of AMBs; they deal with situations where the Case A and B performances have significant differences that can be easily detected in the future laboratory tests. The prototypes' characteristics were measured, in the SI system; the geometric dimensions are $b = 0.137, d = 0.203, q = 0.252, r = 0.060$; the inertia and viscous values are $m = 0.001, I_z = 0.0017, I_x = I_y = J = 0.0592, C_a = 0.0303$. A base current $i_0 = 3$ was considered, leading to the magnetic coefficients $k_p^a = 207,738, k_i^a = 27.70$ for Type A and four-times those values for Type B: $k_p^b = 830,952, k_i^b = 110.79$ (SI units). Assuming a constant angular velocity $\omega = 3400$ rpm, corresponding to 356 rad/s, the state space parameters A, B and D were calculated for Types A and B, generating matrices A_a, A_b , etc. The open-loop behavior of both types is described by the eigenvalues of the system matrices, listed in Table 1, and is clearly unstable.

Table 1. The dynamic behavior of the open loop situation depends on the eigenvalues of A_a and A_b , listed below for Cases A and B. Notice that the stable eigenvalues in Case B are located far to the left.

Open Loop Eigenvalues	
case A	case B
A_a	A_b
$-256.84 \pm j5.12$	$-513.50 \pm j5.11$
$+256.33 \pm j5.11$	$+512.99 \pm j5.11$

A linear quadratic regulator (LQR) control law was used to stabilize the prototypes. The same performance defining parameters were used for both cases: identity matrices $Q = I_4$ and $R = I_2$. The resulting gain matrices:

$$F_a = \begin{bmatrix} -10119 & -202 & -39 & 0 \\ 202 & -10119 & 0 & -39 \end{bmatrix} \quad \text{and} \quad F_b = \begin{bmatrix} -10122 & -101 & -20 & 0 \\ 101 & -10122 & 0 & -20 \end{bmatrix}$$

are to be used in the state feedback control laws $u = F_{a,b}x$. The numerical values in the matrices above are close, meaning that the control efforts can be considered similar in Cases A and B. The closed-loop dynamic behavior can be described by the eigenvalues of $A + BF$, listed in Table 2.

Table 2. The dynamic behavior of the closed loop situation depends on the eigenvalues of $A + BF_{ab}$, listed below for Cases A and B. Notice that the eigenvalues in Case B are located far to the left.

Closed Loop Eigenvalues	
case A	case B
$A_a + B_a F_a$	$A_b + B_b F_b$
$-263.18 \pm j5.24$	$-539.93 \pm j5.37$
$-250.16 \pm j4.98$	$-487.88 \pm j4.85$

Both cases present a highly damped behavior (very small imaginary part in the eigenvalues). Case B is noticeable faster. The response of Cases A and B to $x_s(0) = 0.0002$ (0.2 mm), $y_s(0) = -0.0002$ and zero initial velocities was simulated. Figures 12 and 13 show $x_s(t)$ and $y_s(t)$ in Cases A and B. Notice that the time scales are different and that Case B is at least two-times faster than Case A. If curves for the required control efforts u were drawn, the simulations would again show a much faster performance for Type B.

For evaluating the prototypes' disturbance characteristics, simulations were made for an extra mass of 1 g fixed in the upper disk. The rotor will be unbalanced, and harmonic forces will appear at the x and y axes. The resulting disturbance torques will impose orbital movements on the rotor. This means that, for the same initial conditions, the radial displacements will not tend to zero anymore. Figure 14 shows x_s plotted against y_s for Types A (at the left) and B, where the orbits are smaller, characterizing a stiffer suspension behavior, as expected.

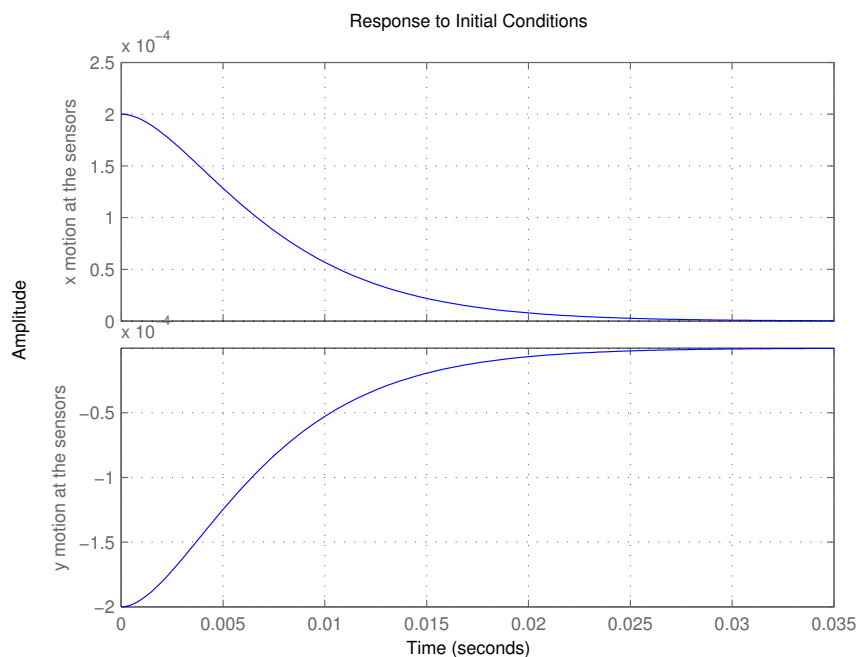


Figure 12. Case A stabilized by F_a : curves for x_s and y_s when $x_s(0) = 0.0002$, $y_s(0) = -0.0002$ and the initial velocities are zero. For $t \geq 0.035$ s, the rotor can be considered centered.

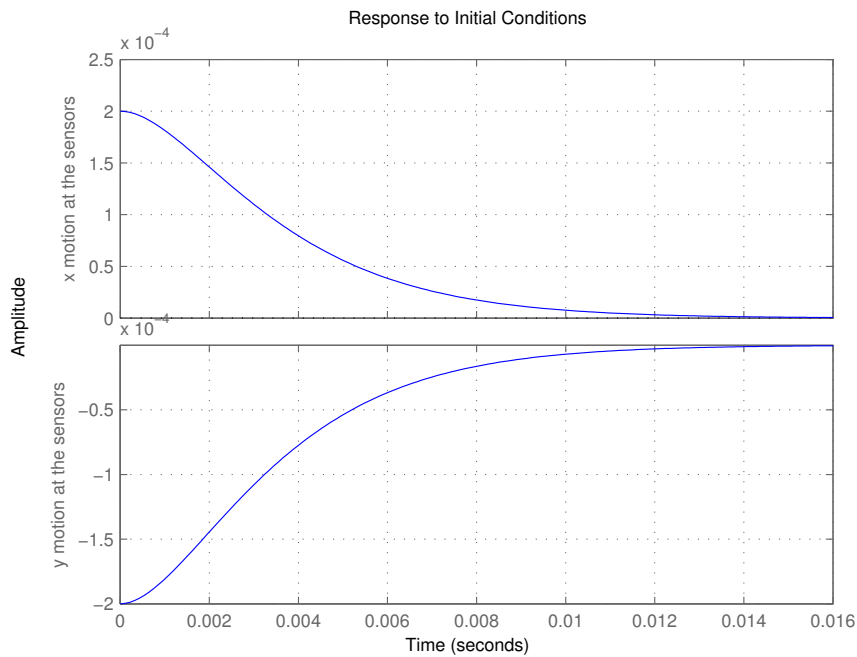


Figure 13. Case B stabilized by F_b : curves for x_s and y_s when $x_s(0) = 0.0002$, $y_s(0) = -0.0002$ and zero initial velocities. The rotor can be considered in position for $t \geq 0.016$ s, half the time of Case A.

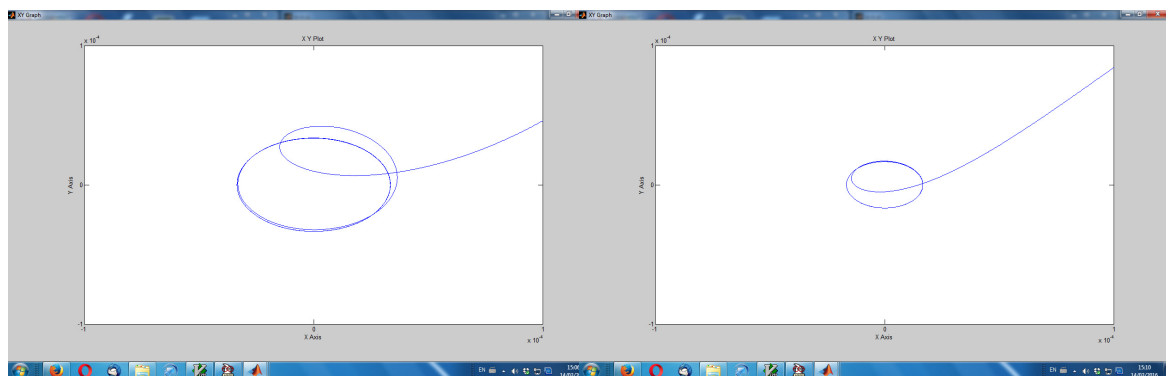


Figure 14. Rotor orbital movements due to harmonic disturbances caused by a mass unbalance in the upper disk; Case A on the left and Case B on the right. The scales for the horizontal (x_s) and vertical (y_s) axes in both the left and right graphs range from -10^{-4} to 10^{-4} m.

These simulations suggest a procedure for laboratory tests on the prototypes: measuring the orbits. In addition to this, a frequency response test was presented in [13] and is repeated here. Assuming now a constant $\omega = 100$ rad/s (954 rpm), the state space parameters A, B and D are calculated, generating matrices A_a, A_b , etc. A state feedback control law $u = Fx$ capable of stabilizing both models can be achieved with:

$$F = \begin{bmatrix} -6073.8 & -25.5 & -3.5 & 0 \\ 25.5 & -6073.8 & 0 & -3.5 \end{bmatrix}.$$

The resulting closed-loop is described by the eigenvalues of $A_a + B_a F = \{-22.2 \pm j113.8, -24.5 \pm j110.9\}$ and $A_b + B_b F = \{-90.1 \pm j211.5, -95.2 \pm j211.5\}$. Simulations, with F driving models (A_a, B_a) and (A_b, B_b) (calculated for a fixed $w = 100$ rad/s) show

that both cases are very quickly stabilized, in less than a second. With an extra mass of 1 g fixed in the upper disk, the resulting harmonic forces will impose orbital movements on the rotor, and the overall efficiency of the AMB control can be judged by these orbits, as noted above. A more complex simulation, with the model parameters now depending on ω (A_{21} and D_2 in (44) and (45)), can be performed. For the same stabilizing F above, and for ω slowly varying from the rest condition to 250 rad/s, the orbit radius for Cases A and B was plotted as function of ω ; the results are shown in Figure 15.

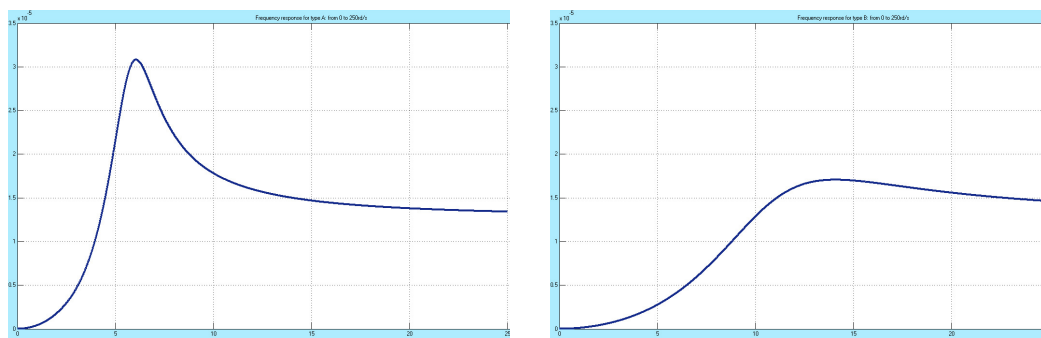


Figure 15. Steady state orbit radius as function of the exciting frequency; the effects are due to harmonic disturbances caused by a mass unbalance in the upper disk. Case A on the left and Case B on the right; the frequency ω in the horizontal axes varies from rest to 250 rad/s, the vertical scales range from 0 to 3.5×10^{-5} m. The high resonance in Case A almost disappears in Case B.

The sharp resonance in Model A is almost completely eliminated and shifted to a higher frequency, in Case B. Other control laws $u = Fx$ can be found that stabilize both models with a better dynamic behavior that avoids resonances in their frequency response. In all of these simulations, Model B offers a clearly superior disturbance rejection characteristic. The bench tests to be made with the real prototypes can follow very closely the procedures used in these simulations.

As a final remark, it must be said that the control laws presented in this section are “special purpose” ones: their main goal is to stabilize the prototypes in a way that the differences between Types A and B are explicitly shown and enhanced. The extremely important problem of choosing control laws for the normal operation of AMBs, either of Type A or B, does not fit in this paper; it belongs to a more control-oriented publication, where lengthy discussions could be made. This future paper could address, for instance, the interesting problem of, with the help of control, making a Type A bearing behave like a Type B.

6. Comments and Conclusions

A detailed mathematical model for Type B is the main contribution of this paper. Its validity, as well as many possible comparisons with Type A, must wait for practical tests. The prototypes are already finished and operational, but no solid measurements have been made up to now. The simulations shown previously confirm the basic assumptions of Type B superiority, but, more than that, they suggest the laboratory procedures to be used in the actual testing of the prototypes.

Some pertinent questions, not treated in this paper, but that will be certainly the object of future research, must be considered. Is the Type B configuration, with its interconnected fluxes, decoupled actions and higher magnetic gains as easy to control with traditional methods as Type A? Are there control laws capable of imposing a Type B behavior on a Type A bearing? Can higher values for k_p and k_i bring undesired effects, like bearing forces that are more sensitive to external disturbances? Will the linearity be affected, with a narrower operating range?

Some other important facts can be considered in future works. It seems obvious that a Type B structure, with only four “poles”, is more compact and, therefore, easier to design and build; its heat

dissipation and magnetic loss characteristics are also expected to be superior. If these conjectures are confirmed on the future laboratory tests, a solid advantage for Type B would appear.

Acknowledgments: The authors would like to thank the anonymous reviewers for many pertinent comments and suggestions. The authors would also like to thank FAPERJ and CNPq for the financial support in the prototypes construction.

Author Contributions: The first two authors have worked for a long time in the split-winding self-bearing motors research area in Brazil. Following an idea from the first author, all the theoretical aspects of that field could be applied to AMBs. The third author is responsible for the simulations and control contents of the article. All authors reviewed and depured the final text.

Conflicts of Interest: The authors declare no conflict of interest.

References

1. Schweitzer, G.; Bleuler, H.; Traxler, A. *Active Magnetic Bearings*; Hochschulverlag AG an der ETH Zürich: Zürich, Switzerland, 1994.
2. Chiba, A.; Fukao, T.; Ichikawa, O.; Oshima, M.; Takemoto, M.; Dorrell, D. *Magnetic Bearings and Bearingless Drives*; Newnes-Elsevier: Amsterdam, The Netherlands, 2005.
3. Schweitzer, G.; Maslen, E.; Bleuler, H.; Cole, M.; Keogh, P.; Larsonneur, R.; Nordmann, R.; Ogada, Y. *Magnetic Bearings: Theory, Design and Applications to Rotating Machinery*; Springer: Berlin/Heidelberg, Germany, 2009.
4. Santisteban, J.A.; David, D.F.B.; Noronha, R.; Ripper, A.; Stephan, R.M. Controller Design for a Bearingless Electric Motor. In Proceedings of the 7th International Conference on Dynamic Problems in Mechanics (DINAME'97), Angra dos Reis, Brazil, 3–7 March 1997; pp. 169–171.
5. Nicolsky, R.; Gorelov, Y.; Pereira, A.S.; David, D.F.B.; Santisteban, J.A.; Stephan, R.M.; Ripper, A.; de Andrade, R., Jr.; Gawalek, W.; Habisreuther, T.; et al. Superconducting Axial Bearing for Induction Machines with Active Radial Magnetic Bearings. *IEEE Trans. Appl. Supercond.* **1999**, *9*, 964–967.
6. David, D.F.B. Levitação de Rotor por Mancais-Motores Radiais Magnéticos e Mancal Axial SC Auto-Estável. Ph.D. Thesis, Universidade Federal do Rio de Janeiro, Rio de Janeiro, Brazil, 2000. (In Portuguese)
7. Nicolsky, R.; de Andrade, R., Jr.; Ripper, A.; David, D.F.B.; Santisteban, J.A.; Stephan, R.M.; Gawalek, W.; Habisreuther, T.; Strasser, T. Superconducting Electromagnetic Hybrid Bearing Using YBCO Bulk Blocks for Passive Axial Levitation. *Supercond. Sci. Technol.* **2000**, *13*, 1–5.
8. David, D.F.B.; Gomes, A.C.D.N.; Santisteban, J.A.; Ripper, A.; de Andrade, R., Jr.; Nicolsky, R. A Hybrid Levitating Rotor with Radial Electromagnetic Motor-bearings and Axial SC Bearing. In Proceedings of the 16th International Conference on Magnetically Levitated Systems and Linear Drives (MAGLEV 2000), Rio de Janeiro, Brazil, 7–10 June 2000; pp. 441–446.
9. David, D.F.B.; Santisteban, J.A.; Gomes, A.C.D.N.; Nicolsky, R.; Ripper, A. Dynamics and Control of a Levitating Rotor Supported by Motor-Bearings. In Proceedings of the 10th International Conference on Dynamic Problems in Mechanics (X DINAME), Ubatuba, Brazil, 10–14 March 2003; pp. 283–288.
10. Rodriguez, E.F.; Santisteban, J.A. An Improved Control System for a Split Winding Bearingless Induction Motor. *IEEE Trans. Ind. Electron.* **2011**, *58*, 3401–3408.
11. David, D.F.B.; Santisteban, J.A.; Gomes, A.C.D.N. Interconnected Four Poles Magnetic Bearings. In Proceedings of the 1st Brazilian Workshop on Magnetic Bearings, Rio de Janeiro, Brazil, 25–26 October 2013.
12. David, D.F.B.; Santisteban, J.A.; Gomes, A.C.D.N. Interconnected Four Poles Magnetic Bearings Simulations and Testing. In Proceedings of the 14th International Symposium on Magnetic Bearings (ISMB14), Linz, Austria, 11–14 August 2014; pp. 30–35.
13. David, D.F.B.; Santisteban, J.A.; Gomes, A.C.D.N. Laboratory Tests on an Interconnected Four Poles Magnetic Bearing. In Proceedings of the 15th International Symposium on Magnetic Bearings (ISMB15), Kitakyushu, Japan, 3–6 August 2016.
14. Krodkiewski, J.M.; Zmood, R.B. Use of Programmed Magnetic Bearing Stiffness and Damping to Minimize Rotor Vibrations. In Proceedings of the 3rd International Symposium on Magnetic Bearings (ISMB3), Charlottesville, VA, USA, 29–31 July 1992.

15. Kjølhed, K.; Santos, I.F. Experimental Contribution to High-Precision Characterization of Magnetic Forces in Active Magnetic Bearings. *J. Eng. Gas Turbines Power* **2007**, *129*, 503–510.
16. Imlach, J. High Specific Load Capacity Radial Magnetic Bearing Actuator. U.S. Patent No. 5,962,940, 5 October 1999.



© 2017 by the authors. Licensee MDPI, Basel, Switzerland. This article is an open access article distributed under the terms and conditions of the Creative Commons Attribution (CC BY) license (<http://creativecommons.org/licenses/by/4.0/>).